

PROPENSITY OF WATER SELF-IONS AT AIR(OIL)-WATER INTERFACES REVEALED BY DEEP POTENTIAL MOLECULAR DYNAMICS WITH ENHANCED SAMPLING

Pengchao Zhang¹, and Xuefei Xu^{1,*}.

¹Center for Combustion Energy, Department of Energy and Power Engineering, and Key Laboratory for Thermal Science and Power Engineering of Ministry of Education, Tsinghua University, Beijing 100084, China

*Corresponding author e-mail: xuxuefei@tsinghua.edu.cn

ABSTRACT

The preference of water self-ions (hydronium and hydroxide) towards air/oil-water interfaces is one of the hottest topics in water research due to its importance for understanding properties, phenomena, and reactions of interfaces. In this work, we performed enhanced-sampling molecular dynamics simulations based on state-of-the-art neural network potentials with approximate M06-2X accuracy to investigate the propensity of hydronium and hydroxide ions at air/oil(decane)-water interfaces, which can simultaneously describe well the water autoionization process forming these ions, recombination of ions, and ionic distribution along the normal distance to the interface by employing a set of appropriate Voronoi collective variables. A stable ionic double-layer distribution is observed near the air-water interface, while the distribution is different at oil-water interfaces, where hydronium tends to be repelled from the interface into the bulk water, whereas hydroxide, with an interfacial stabilization free energy of -0.6 kcal/mol, is enriched in the interfacial layer. Through simulations of oil droplets in water, we further reveal that the interfacial propensity of hydroxide ions is caused by the positive charge distribution of the oil-water interface contributed by hydrogens of the dangling OH bonds of interfacial water layer and the outmost layer decane molecules laying flat on the droplet. The present results may aid in understanding the acid-base nature of water interfaces with wide applications.

1 Introduction

Water interfaces play a crucial role in both natural sciences and engineering applications due to providing fundamental heterogeneous environments.^{1–3} The preferential accumulation of water self-ions at these interfaces, namely hydroxide (OH^-) and hydronium (H_3O^+), can impact both interfacial properties^{4,5} and chemical reaction processes,^{5–7} and has been widely investigated. Nevertheless, the propensity of self-ions enriching at air-water and oil-water interfaces continues to be an open question due to contradictory findings from these previous studies.^{8–12}

For example, the macroscopic experiments measured the negative zeta potential of air bubbles^{13–16} and oil droplets^{15,17,18} in water and inferred the enrichment of OH^- at the air(oil)-water interfaces considering that OH^-

is the only anionic source in pure water. The second harmonic generation¹⁹ and sum-frequency vibrational spectroscopy^{20,21} studies also provided microscopic evidence for the adsorption of OH^- at the oil-water interface. However, spectroscopic measurements of air-water interfaces observed the interfacial enhancement of H_3O^+ .^{8,22–24} Similarly, microscopic simulations also obtained conflicting conclusions on the interfacial excess of self-ions. Most microscopic studies found that H_3O^+ ions tend to accumulate at the top layer of air-water interfaces,^{9,25–30} while OH^- ions are repelled into the water bulk^{27,28} or show no preference.³¹ A few studies observed that OH^- ions, rather than H_3O^+ , slightly accumulate at the air-water interfaces.^{32–34}

Our recent deep potential molecular dynamics (DPMD) simulations on ionic distribution provide a possible explanation for the inconsistency of these conclusions at the air-water interface³⁵ and nitrogen-water interface.³⁶ We found an interfacial double-layer distribution of water self-ions.³⁵ In this distribution, H_3O^+ predominantly occupies the top layer of the interface, while OH^- is enriched in the deeper interfacial layer below that of H_3O^+ . Compared to H_3O^+ , OH^- has a more negative free energy of interfacial stabilization and accordingly a higher interfacial concentration, leading to negatively charged interfaces and negative zeta potential. These results are consistent with the macroscopic detection and do not contradict microscopic observation, as the previous conflicting results may be caused by measuring at different or ambiguous interfacial depths. And this finding has been further evidenced by a high-level heterodyne-detected vibrational sum frequency generation (vSFG) study.³⁷ However, it is important to note that our previous work performed separate simulations for OH^- and H_3O^+ , without considering their origins and recombination at the interface. Therefore, in this work, we performed further investigation with the corresponding consideration to validate the observation of the double-layer distribution.

Technically, it is pretty demanding to simulate the water autoionization reaction of forming OH^- and H_3O^+ , because it is an exceedingly rare event. Dynamics studies on the process in bulk water have been conducted for decades.^{38–44} Recently, there was significant progress in accurate simulations of the water autoionization reaction and pK_w ,^{45–48} benefiting primarily from the developments in neural network potentials and enhanced sampling methods. Here, we utilized the on-the-fly probability enhanced sampling (OPES) method^{49,50} with a set of Voronoi collective variables (CVs)^{51–53} to sample this rare event efficiently, and we employed neural network potential models with approximate M06-2X⁵⁴ accuracy to drive MD simulations. Armed with these state-of-the-art methods, we obtained the free energy of water autoionization in quantitative agreement with experimental observations. Most significantly, the present deep-going investigation confirms the phenomenon of the ionic double-layer distribution at the air-water interface with the full consideration of water autoionization and its reverse recombination processes. In addition, we extended our study to oil-water (decane-water) interfaces, and observed a totally distinct distribution of water self-ions, where OH^- ions preferentially accumulate near the decane-water interface, while H_3O^+ ions are repelled into the bulk.

2 Results and discussion

2.1 Water autoionization

Before discussing ionic preferences at interfaces, it is important to validate the feasibility of our methodologies for accurately describing the water autoionization and its reverse process. We first need an efficient potential with an accuracy approaching hybrid meta-GGA functional M06-2X.⁵⁴ We chose to learn the energies and forces of the M06-2X functional because of its reported accuracy in modeling liquid water⁵⁵ and van der Waals interactions.⁵⁶ To expedite this step, we initially trained a deep Kohn-Sham (DeePKS) model^{57–59} with the precision of M06-2X, which saves approximately nine times more time than the regular M06-2X calculations. Then, we trained a deep potential (DP) model using the DeePMD-kit package^{60,61} to closely match the accuracy of the DeePKS model, i.e., the trained DP model would have an approximate M06-2X accuracy. Finally, molecular dynamics simulations were run by using the DP model, which offers a time-saving of more than five orders of magnitude when compared to the conventional *ab initio* MD (AIMD) simulations directly using the M06-2X.

In the simulation, to efficiently sample the rare event of water autoionization, we employed the OPES method. In this way, appropriate CVs must be defined. To depict both the production of OH^- and H_3O^+ by the water autoionization and the diffusion of these self-ions through the Grotthuss mechanism,^{35,62,63} we tessellated the space into Voronoi polyhedra centered on all oxygen atoms and summed up the atomic charges within each polyhedron,^{51–53} that can enable us to automatically identify charge defects of OH^- and H_3O^+ without a priori knowledge, and accordingly designed CVs, which are self-ion number s_a

$$s_a = \sum_{i=1}^{\text{Num}_O} \delta_i^2, \quad (1)$$

self-ion distance s_t

$$s_t = - \sum_{i=1}^{\text{Num}_O} \sum_{j>i}^{\text{Num}_O} r_{i,j} \delta_i \delta_j, \quad (2)$$

and its variant s'_t

$$s'_t = \begin{cases} \log(s_t + \epsilon), & 0 \leq s_t < 1, \\ s_t - 1 + \log(1 + \epsilon), & s_t \geq 1, \end{cases} \quad (3)$$

to distinguish the water autoionization process. The charge defect of the i th Voronoi center (O atom) is denoted by δ_i , with values 0, 1, and -1 for H_2O , H_3O^+ , and OH^- respectively. Distance between two Voronoi centers is represented by $r_{i,j}$. Consequently, the CV s_a signifies the number of H_3O^+ and OH^- ions resulting from water autoionization, while the CV s_t indicates the

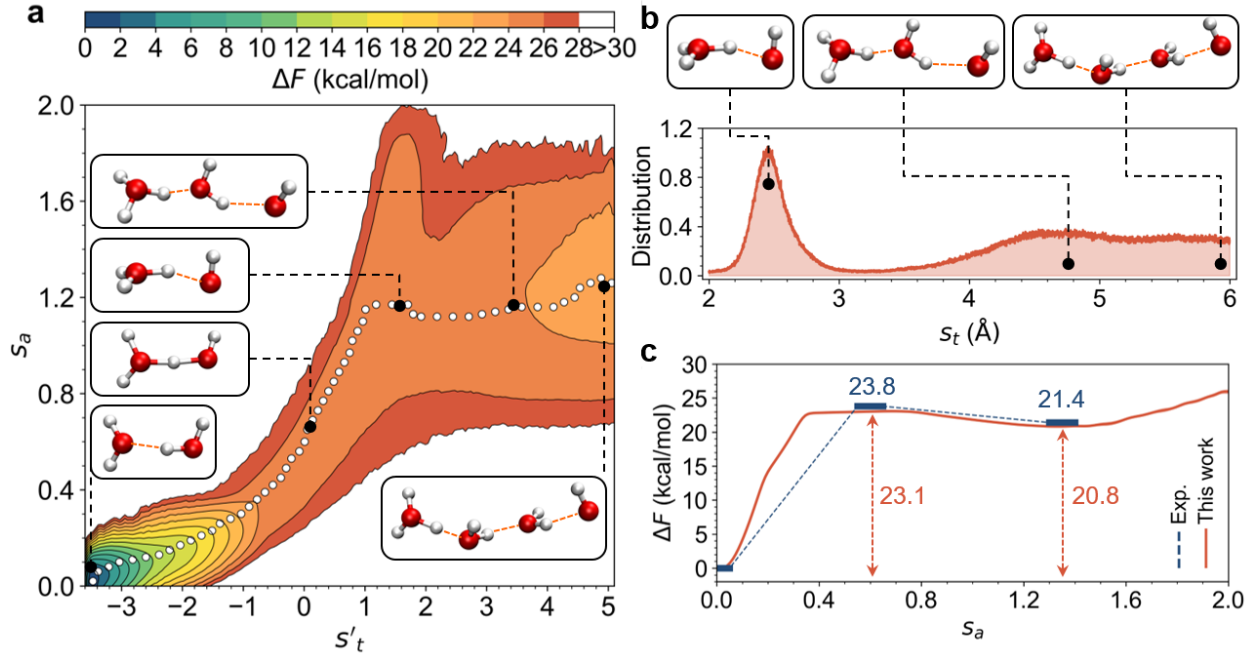


Figure 1: **Free energy surface of water autoionization.** **a.** Two-dimensional FES as a function of the logarithmic variant of ionic distance s'_t and the ionic number s_a , where the minimum free energy path of autoionization is represented by the white dot line. Key structures along the potential optimal pathway of water autoionization are provided, in which surrounding water molecules are hidden. Color code: hydrogen, white; oxygen, red. **b.** Distribution of self-ion distance s_t in product region and corresponding structures of ion pairs. **c.** One-dimensional projection of the FES along the ionic number coordinate s_a . Experimental values are also provided for comparison.

distance between two ions. However, the CV s_t struggles to differentiate between pure water and transition states, so we introduced its logarithmic variant CV s'_t to address this issue. In the definition of s'_t (eq 3), the ϵ is a regularization parameter and is set as 0.03. More details of CVs and other simulation settings are provided in the Supporting Information (SI).

Based on the DPMD simulations, we calculated the free energy surface (FES) as a function of the two defined CVs (s_a and s'_t). As shown in Figure 1a, a deep well is located at $s_a = 0$ and $s'_t = -3.6$ ($s_t = 0$ Å) which presents the neutral water molecules bonded with the hydrogen bonds, namely, the reactant of water autoionization reaction. We also observed a shallow well at $s_a = 1.3$ and $s'_t = 4.8$ corresponding to the autoionization products (OH^- and H_3O^+) separated by a water wire with a length of ~ 6 Å that indicates the metastability of self-ions pair.^{46,64} We further identified the optimal path connecting the two wells and marked it with the white dot line in Figure 1a, accompanied by the key structures along the path. It is revealed that the water autoionization occurs via the concerted transfer of multiple protons along the water wire, which follows the Grotthuss mechanism,^{43,44} in-

volves sequentially a contact OH^- and H_3O^+ ion pair (corresponding to a self-ion distance $s_t = 2.5$ Å in Figure 1b) and a one H_2O -bridged ion pair ($s_t = 4.8$ Å in Figure 1b), and eventually forms the autoionization products, OH^- and H_3O^+ ions separated by a water wire longer than ~ 6 Å.

By projecting the FES along the self-ion number CV, s_a , we got a one-dimensional free energy curve (Figure 1c) to clearly show the free energy change of the reaction process. From Figure 1c, the activation free energy (ΔF^\ddagger) and the reaction free energy (ΔF°) of the water autoionization reaction are estimated as 23.1 and 20.8 kcal/mol, respectively, which are in good agreement with the experimental measurements ($\Delta F^\ddagger = 23.8$ kcal/mol, $\Delta F^\circ = 21.4$ kcal/mol).^{38,40,41} The reverse process—recombination of self-ions, may occur by overcoming a low barrier of approximately 2.3 kcal/mol, which is close to the proton transfer barrier (2.4 kcal/mol) observed in NMR experiments.⁶⁵ These results demonstrate the accuracy of our simulations in characterizing the potential energy landscape of water autoionization.

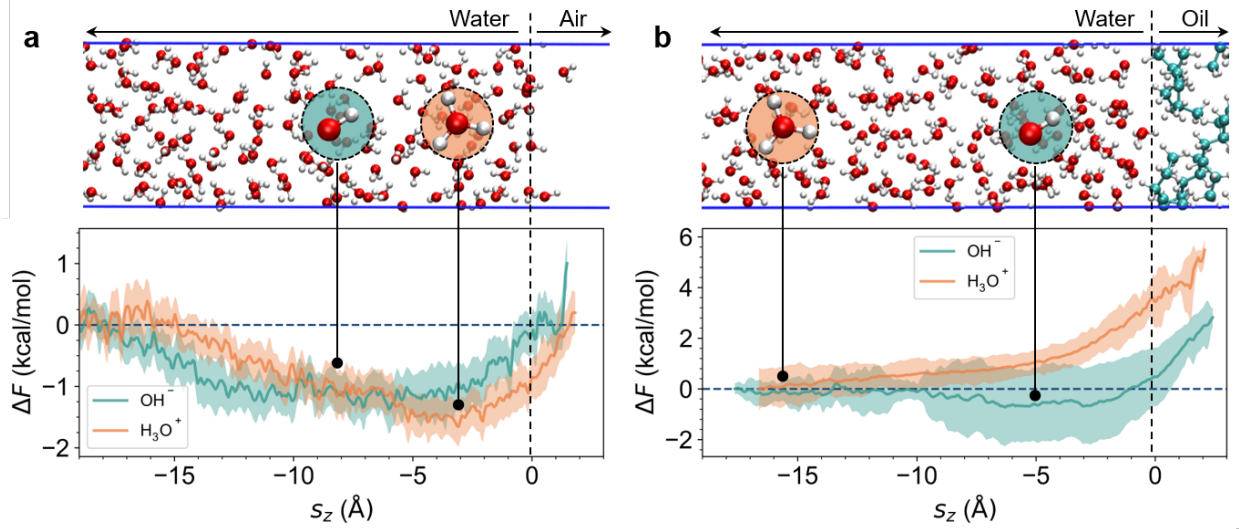


Figure 2: **Distribution of water self-ions near the interface.** One-dimensional free energy curves along the normal distance to **a.** the air-water slab interface and **b.** the oil-water slab interface are depicted below the corresponding schematic diagrams. The values of CV s_z , representing the normal distances to the reference surface, are negative on the water side, zero at the surface, and positive on the air or oil side. In the schematic diagrams, particular emphasis is placed on highlighting the distinct preferential distribution of OH^- and H_3O^+ ions near the interface. Color code: hydrogen, white; oxygen, red; carbon, green.

2.2 Preference of water self-ions towards air(oil)-water slab interfaces

Having validated the accuracy of the methodologies, we shifted our focus to investigating the distribution preference of water self-ions near the air-water and oil-water (decane-water) interfaces. Note that we consider pure water without directly adding any ions in these simulations, and the self-ions are the products of water autoionization. To this end, in the simulations we introduced a new CV s_z

$$s_z = \sum_{i=1}^{\text{Num}_O} \delta z_i \delta_i^2, \quad (4)$$

where δz indicates the relative coordinate along the z -axis. Thus, the CV s_z can describe depths of OH^- (for $\delta_i < 0$) and H_3O^+ (for $\delta_i > 0$) relative to the interfaces. The free energy curves of OH^- and H_3O^+ distribution as the function of s_z were calculated and plotted in Figure 2, where we took the position of the interface as the zero point of s_z for a better understanding of the relative locations to the interface. In this work, the interface of the air-water system is defined to be the surface where the water density is half of its bulk value, and the interface of the oil-water system is set as the surface with the minimum density of the system considering the hydrophobicity of oil. Negative values and positive values of s_z denote the water phase and air (or oil) phase, respectively.

Figure 2a supports the double-layer distribution of water self-ions near the air-water interface. We can clearly see

two free energy wells located at different depths near the interface, which represent the preferential locations of OH^- and H_3O^+ , respectively. The free energy well of H_3O^+ spans the region ($-15 \text{ \AA} < s_z < 1 \text{ \AA}$) near the interface, with the minimum (-1.6 kcal/mol) located at $s_z = -3 \text{ \AA}$; the free energy well of OH^- appears in a deeper layer spanning a wider region ($-18 \text{ \AA} < s_z < 0 \text{ \AA}$) below the interface, and the corresponding minimum has a free energy of -1.3 kcal/mol located at $s_z = -8 \text{ \AA}$. (Note, the reported free energies here are the relative values to the bulk.) The energy well of H_3O^+ near the air-water interface is slightly deeper than that of OH^- , with a difference of 0.3 kcal/mol at the air-water interface, that is opposite to the earlier work³⁵ which yielded a difference of -0.3 kcal/mol between the interfacial stabilization energies of H_3O^+ and OH^- . This discrepancy may arise from the improved sampling methods and potential accuracy in the present work. Nevertheless, the current simulation results reproduce the double-layer distribution of H_3O^+ and OH^- reported in the earlier work,³⁵ as well as their relative locations.

The distribution of water self-ions at the oil-water interface differs from that at the air-water interface, as shown in Figure 2b. The H_3O^+ ions dislike the oil-water interface, with the gradual free energy increases up to 3.4 kcal/mol from the bulk water ($s_z = -16 \text{ \AA}$) to the interface ($s_z = 0 \text{ \AA}$). In contrast, the free energy well of OH^- appears in

the region ($-9 \text{ \AA} < s_z < -1 \text{ \AA}$) near the interface, with the corresponding minimum of -0.6 kcal/mol located at $s_z = -5 \text{ \AA}$. This observation could account for the frequent detection of negative zeta potentials in cases involving oil droplets.^{15,17,18,66}

Combining the above simulation results of air-water and oil-water interfaces, we speculate that the experimental measurements of ionic preference at water interfaces using various experimental spectroscopic techniques^{21,23,24,67,68} contradicted each other that might be caused by that they were probing different depths of the interfacial region or by the insufficient resolution. For instance, vSFG techniques, which provide information solely in the non-centrosymmetric region,⁶⁹ may not effectively detect the distribution of ions in the deeper interfacial layer and specify the interfacial depth.^{70,71} *Ab initio* MD simulations are usually too time-consuming to afford calculating on scales larger than nanometers, while the simulations using small periodic boxes may lead to a loss of information. Our previous DPMD simulations have addressed this issue by achieving *ab initio* level accuracy with linear scaling relative to the number of atoms;^{35,36} however, they still encounter challenges in fully sampling water self-ions in neutral systems. The present work employs enhanced sampling DPMD simulations to effectively tackle these challenges, enabling us to accurately identify the distinct distributions of water self-ions along the interfacial depth.

2.3 Distribution of water self-ions near the oil droplet in water

To explain why water self-ions exhibit different preferences near the oil-water interface compared to the air-water interface, we constructed an oil (decane) droplet with a radius of $\sim 14 \text{ \AA}$ surrounded by over 5,000 water molecules to gather more information on the nanometer spatial scale. We conducted separate simulations for the oil droplet systems containing H_3O^+ and OH^- ions, since this approach can provide at least qualitatively consistent results with simulations using the OPES method and Voronoi CVs for ionic distribution at the air-water interface as validated in the above section and the latter is time-consuming when dealing with thousands of water molecules.

The spatial distribution analysis of H_3O^+ and OH^- ions in water surrounding the oil droplet is illustrated in Figure 3a. This analysis shows that OH^- ions preferentially accumulate near the oil-water interface, with a pronounced peak of the volume-normalized number distribution in the region from -5 to 0 \AA relative to the interface. Figure 3c shows a representative snapshot that illustrates the enrichment of OH^- ions near the oil-water interface. In contrast, H_3O^+ ions exhibit a flat distribution from -12 to

-7 \AA , showing a weak propensity to be away from the oil-water interface (Figure 3b). As we have expected, these results are consistent with our free energy calculations based on the enhanced sampling DPMD simulation in an oil-water slab system in the section 2.2, which reveal that only OH^- ions have a preference towards the oil-water interface.

We further analyze the ionic orientation and hydrogen bonding network in the oil droplet system. For H_3O^+ ions preferentially distributed in the bulk water, their dipole vectors are distributed randomly, with $\cos \theta$ ranging from -1.0 to 1.0 , where the θ is the angle between the normal vector of interface and the ionic dipole vector (Figure 3d,e). The hydrogen bond (HB) number per H_3O^+ ion in water is primarily three, that is, the three hydrophilic protons of H_3O^+ act as donors, forming three HBs with neighboring water molecules (Figure 3f). Figure 3d shows that OH^- ions enriched in the oil-water interface are predominantly aligned anti-parallel to the interfacial normal vector, with $\cos \theta$ around -1.0 , indicating that interfacial OH^- ions are mainly dangling on the water surface with hydrogen towards the oil side. Thus, the hydrogen cannot act as an HB donor anymore, and the interfacial OH^- forms fewer hydrogen bonds (around 4, mainly by oxygen with more lone pair electrons as HB acceptors) as compared to those (around 5) distributed in the water bulk, as shown in Figures 3c,f). Yang et al.²¹ have ever observed the accumulation of OH^- ions at the hydrophobic hexane-water interface but they attributed the interfacial stability of OH^- to hexane-incorporated HB network, in which a hypercoordinated structure of OH^- is formed with a larger average number of HBs than OH^- in the bulk water. In contrast, we barely observe the weak hydrogen bonds formed between decane and OH^- ions in the present decane droplet system. This inconsistency may arise from the constructed model systems. Yang et al.²¹ modeled a monolayer hexane gas-water system where the hexane molecules are adsorbed on the water surface by the Van der Waals interaction, while we modeled a decane droplet in water where the surface tension of droplet may affect the interfacial molecular interaction.

We next analyze the radial distribution of atomic partial charge⁷² for the oil droplet in pure water and the preferred orientation of interfacial water and decane molecules. The Hirshfeld charge was effectively predicted by training a deep charge (DC) model^{73,74} with the M06-2X method. More details on the training can be found in the SI.

From the droplet center (14 \AA) to the droplet surface (0 \AA), a staggered distribution of positive and negative charge density is observed, as depicted in Figure 4a. This

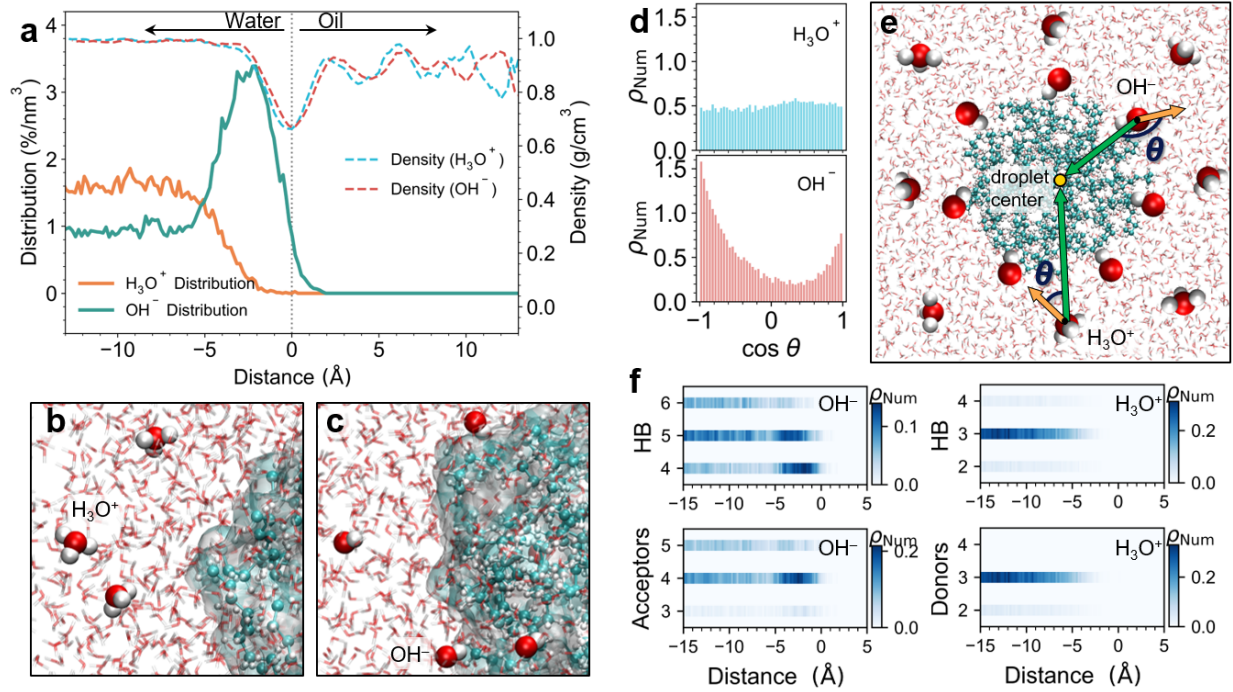


Figure 3: Distribution and hydrogen bonding network of water self-ions near the oil-water interface. **a.** The volume-normalized number distribution (solid lines) of OH^- and H_3O^+ ions along the normal distance to the oil-water interface and the total density of systems (dashed lines) that contain OH^- or H_3O^+ ions. The spherical surface with the minimum density of system is defined as the oil-water interface. The normal distance is set as negative in the water region, zero at the oil-water interface, and positive in the oil droplet region. **b.** and **c.** Typical snapshots showing the repulsion of H_3O^+ and the accumulation of OH^- ions near the oil-water interface. **d.** Orientation distributions of OH^- (counted from -5 to 0 Å) and H_3O^+ (counted from -12 to -7 Å) in their preferred water layers. The histogram bars represent the cumulative number density, ρ_{Num} , of self-ions within statistical intervals. The orientation of the ions is quantified by the cosine of the θ angle. **e.** Schematic representation of the θ angle between the normal vector (directing from water self-ions to the droplet center, indicated by green arrows) and the dipole vector (directing from the H center to O, illustrated by orange arrows) of the self-ions. **f.** The HB number per ion, as well as the number of HBs acting as acceptors or donors. The color bars indicate the cumulative number density ρ_{Num} within statistical intervals.

phenomenon probably arises from the fact that the decane molecules form the oil droplet by wrapping layer by layer around the droplet center, which is evidenced by the linearly increased $\cos \beta$ distribution from 0 to -1 (Figure 4f) and the $\cos \alpha$ distribution peaking around 0.77 (Figure 4e), where the former indicates that the decane molecules in the droplet are primarily straight chains and the latter shows that the outmost layer decane molecules approximately remain flat on the oil droplet surface indicated by the α angle of 40° as illustrated by Figure 4b. Consequently, along the radial direction, the hydrogen atoms with positive Hirshfeld charge and the carbon atoms with negative Hirshfeld charge appear alternatively, leading to the staggered distribution of total charge density.

At the oil-water interface, which is defined as the position with the smallest density of system and marked by a vertical gray dot line in Figure 4a, there is a peak of positive charge density. Based on the orientation analysis in Figures 4c, d for the interfacial water molecules and the $-\text{CH}_2-$ and $-\text{CH}_3$ groups of interfacial decane, we infer that hydrogens of the dangling OH bonds of interfacial water layer and most hydrogens of the outmost layer decane molecules collaboratively contribute to this interfacial positive charge density peak (Figures 4b). The positive charge distribution at the oil-water interface may attract the OH^- ions and repel H_3O^+ ions. In the bulk water region ranging from -13 to -2 Å, the system approaches a nearly neutral charge density. (Figure 4a).

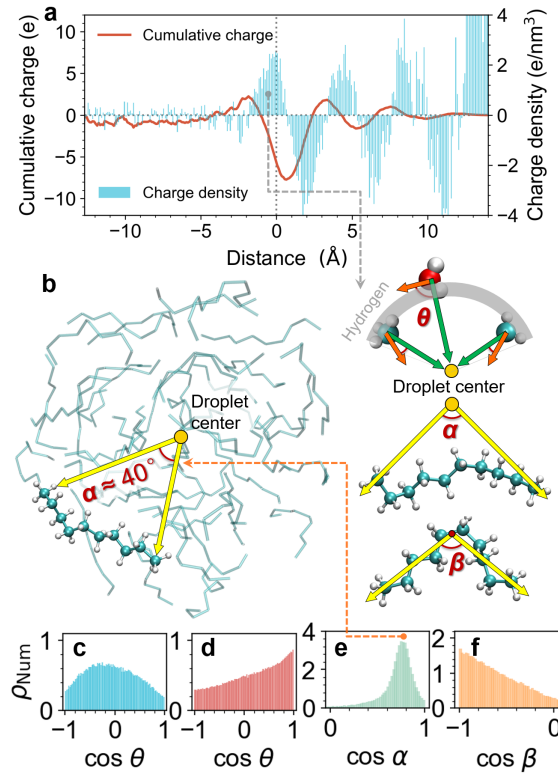


Figure 4: **Charge distribution of the oil droplet in pure water and the orientation distribution of interfacial water and decane.** **a.** Charge density and cumulative charge as functions of normal distance. The zero of normal distance is the position of interface. **b.** The highlight of a representative decane molecule that remains flat on the oil surface with an angle of $\alpha \approx 40^\circ$, and the schematic diagrams of the angles θ , α , and β . **c-e.** Orientation distributions of interfacial H₂O molecules (distance greater than -0.8 Å), $-\text{CH}_2-$ and $-\text{CH}_3$ groups of decane (distance less than 3 Å), and decane chains. The angle θ (as shown in **b.**) is defined as the angle between the normal vector (extending from the targeted O or C atom to the droplet center) and the dipole vector (ranging from the H center to the O or C atom). The angle α (as shown in **b.**) is the angle between two vectors from the droplet center to the two terminal carbons of decane. **f.** Bending degree of decane chains, estimated by the angle β (as shown in **b.**) between the two vectors from the center of the central C-C bond to two terminal carbons of decane.

By summing the charge from the droplet center toward the water phase, we determine the cumulative charge for statistical spheres with different radii and plot them in Figure 4a using the red solid line. Near the oil-water interface, the cumulative charge reaches a maximum negative value of -2.6 e/nm³ at the normal distance of 0.6 Å, which may explain the experimentally observed negative zeta potentials of oil droplets.^{15,17,18,66} Additionally, the attraction of OH⁻ ions by the interfacial positive charge density may also contribute to the observed negative zeta potentials.

3 Conclusion

In summary, with enhanced sampling techniques that can efficiently sample water autoionization processes and describe well ionic diffusion and recombination, we in-

vestigated the interfacial distribution propensity of OH⁻ and H₃O⁺ in air(oil)-water interfaces by deep potential molecular dynamics simulations. We first validated the double-layer distribution of water self-ions in the air-water interface with H₃O⁺ enriching in the topmost water layer and OH⁻ staying in a few-angstroms deeper layer. Interestingly, we then found that different from the air-water interface, the oil(decane)-water interface attracts OH⁻ but excludes H₃O⁺. To understand the distinct behaviors, we performed the charge analysis and molecular orientation statistics for an oil droplet-water system and discovered that the layer-by-layer arrangement of nearly straight decane molecules around the droplet center allowed oil droplets in water to have staggered positive and negative charge distributions along the radial direction. The resulting positive charge distribution of the oil-water

interface induces the interfacial enrichment of OH^- ions and the interface exclusion of H_3O^+ ions. We also noticed the negative cumulative charge of the oil droplet when involving its nearest neighboring water layer, and we speculated that this negative charge, together with the adsorbed OH^- ions, led to the experimental detection of negative zeta potentials of oil droplets. The present results enrich the knowledge on various water interfaces and offer valuable insights that contribute potentially to their application across multiple fields.

4 Method

4.1 Neural network model training

We aim to train three models: a deep potential (DP) model^{60,61} for molecular dynamics simulations investigating water autoionization and distribution of self-ions along interfaces; a deep Kohn-Sham (DeePKS) model^{57,59} with accuracy comparable to the M06-2X functional, and the DeePKS model will be used for labeling the training data sets of energies and atomic forces needed for training the DP model; and a deep charge (DC) model^{73,74} for predicting atomic partial charges. To ensure diverse and uncorrelated data, we generate multiple independent MD simulations with enhanced sampling on some configuration subsystems (Table S1 in the SI).

The training sets for the three models differ significantly in size due to variations in their descriptors. All models, however, adhere to the criteria of physical symmetry and locality. The DP and DC models incorporate angular and radial atomic environment descriptors, while the DeePKS model includes gauge invariance symmetry and density matrices projected on atomic orbitals.^{57,59,75} Consequently, the DeePKS model requires only a few hundred configurations for training, whereas the DP and DC models necessitate tens of thousands to accurately capture reactive processes as shown in Table S2 in the SI.

4.2 Density functional theory (DFT) calculation

The label preparation of data sets for three models involves M06-2X⁵⁴ calculations for energies and forces using the CP2K package.⁷⁶ These calculations utilize Goedecker-Teter-Hutter pseudopotentials^{77,78} and a QZV3P basis set.⁷⁹ The multi-grid level employs a plane-wave cutoff of 1000 Ry for the total density and 70 Ry for the Kohn-Sham orbitals, as confirmed by a previous convergent test.⁵³ To speed up the convergence of self-consistent field (SCF) iterations, the auxiliary density matrix method is employed.⁸⁰ In addition, the Hirshfeld charge⁷² is also calculated to prepare the data set for training the DC model.

4.3 Molecular dynamics simulations

DPMD simulations are conducted using the LAMMPS software.⁸¹ Prior to simulating the interface systems, the accuracy of water autoionization is assessed through 10 ns *NVT* (constant volume constant temperature) simulations with a 1.0 fs integration time step. For the air-water and oil-water slab systems, 10 ns simulations are conducted to achieve converged results. In the case of the larger oil droplet systems, 3 ns simulations are carried out. Temperature control at 300 K is achieved using a velocity-rescaling thermostat⁸² with a damping time of 0.04 ps in all DPMD simulations. Simulation systems are listed in Table S3 in the SI.

4.4 Enhanced sampling settings

In DPMD simulations for studying the autoionization and the ionic distribution, the OPES method^{49,50,83} with Voronoi CVs is employed.⁵¹⁻⁵³ The CVs, s , effectively capture slow modes and infrequent occurrences by relating them to atomic coordinates. The external bias potential $V(s)$ is incorporated into the system's potential energy during MD simulations using the PLUMED plugin.⁸⁴ In OPES, $V(s)$ at the n th step is characterized by

$$V_n(s) = (1 - \frac{1}{\gamma}) \frac{1}{\beta} \log(\frac{P_n(s)}{Z_n} + \epsilon), \quad (5)$$

which involves the bias factor $\gamma = \beta \Delta E_{\text{bias}}$, inverse Boltzmann factor $\beta = 1/k_B T$, the unbiased marginal distribution probability $P(s)$, and a normalization factor Z . The regularization term $\epsilon = e^{-\gamma/(1-1/\gamma)}$ ensures a positive argument for the logarithm and imposes a bias constraint that confines sampling to the specified region of interest. A value of ΔE_{bias} of 75 kJ/mol is chosen to approximate the free energy barrier of water autoionization.

Based on the DPMD simulation results, the free energy surface along the CV can be calculated as follows

$$F(s) = -\frac{1}{\beta} \log P(s). \quad (6)$$

In the regime of quasi-static bias, $P(s)$ can be reweighted as an average over the biased ensemble.⁴⁹

Comprehensive computational methods and additional details are available in the SI.

Data availability

The simulation and visualization packages used to perform the calculations are freely available. The input files needed to reproduce the research are available at <https://github.com/Zhang-pchao/OilWaterInterface>.

Supporting Information Available

Potential model generation, including construction of training data sets, DFT calculation, and model training for DeePKS model, DP model, and DC models. Molecular dynamics simulations, including those for the data set generation and for studying the autoionization and the ionic distribution. Enhanced sampling settings, including bias potential, definition of collective variables, and free energy calculation. Simulation workflow, schematic diagram of simulation systems, diffusion coefficients, error distribution on test data sets, free energy, orientation distribution, hydrogen bond, and other details (PDF).

Conflicts of interest

The authors declare no competing financial interest.

Acknowledgments

This work was partially supported by the National Natural Science Foundation of China under Grant Nos. [21973053, 11988102]. The authors acknowledge the valuable discussions with Professor Michele Parrinello, Axel Tosello Gardini, and Ling Liu. Computational resources were provided by the High Performance Computing (HPC) platform at Tsinghua University, the HPC Franklin at Fondazione Istituto Italiano di Tecnologia, and the Bohrium Cloud Platform (<https://bohrium.dp.tech>) from DP Technology.

References

- [1] Ruiz-Lopez, M. F.; Francisco, J. S.; Martins-Costa, M. T.; Anglada, J. M. Molecular Reactions at Aqueous Interfaces. *Nat. Rev. Chem.* **2020**, *4*, 459–475.
- [2] Wei, Z.; Li, Y.; Cooks, R. G.; Yan, X. Accelerated Reaction Kinetics in Microdroplets: Overview and Recent Developments. *Annu. Rev. Phys. Chem.* **2020**, *71*, 31–51.
- [3] Bjoörneholm, O.; Hansen, M. H.; Hodgson, A.; Liu, L.-M.; Limmer, D. T.; Michaelides, A.; Pedevilla, P.; Rossmesl, J.; Shen, H.; Tocci, G.; Tyrode, E.; Walz, M.-M.; Werner, J.; Blum, H. Water at Interfaces. *Chem. Rev.* **2016**, *116*, 7698–7726.
- [4] Chamberlayne, C. F.; Zare, R. N. Simple Model for the Electric Field and Spatial Distribution of Ions in a Microdroplet. *J. Chem. Phys.* **2020**, *152*, 184702.
- [5] Martins-Costa, M. T.; Ruiz-López, M. F. Electrostatics and Chemical Reactivity at the Air–Water Interface. *J. Am. Chem. Soc.* **2023**, *145*, 1400–1406.
- [6] Lee, J. K.; Walker, K. L.; Han, H. S.; Kang, J.; Prinz, F. B.; Waymouth, R. M.; Nam, H. G.; Zare, R. N. Spontaneous Generation of Hydrogen Peroxide from Aqueous Microdroplets. *Proc. Natl. Acad. Sci. U. S. A.* **2019**, *116*, 19294–19298.
- [7] Zhong, G.; Cheng, T.; Shah, A. H.; Wan, C.; Huang, Z.; Wang, S.; Leng, T.; Huang, Y.; Goddard III, W. A.; Duan, X. Determining the Hydronium pK_a at Platinum Surfaces and the Effect on pH-dependent Hydrogen Evolution Reaction Kinetics. *Proc. Natl. Acad. Sci. U. S. A.* **2022**, *119*, e2208187119.
- [8] Vácha, R.; Buch, V.; Milet, A.; Devlin, J. P.; Jungwirth, P. Autoionization at the Surface of Neat Water: Is the Top Layer pH Neutral, Basic, or Acidic? *Phys. Chem. Chem. Phys.* **2007**, *9*, 4736–4747.
- [9] Buch, V.; Milet, A.; Vácha, R.; Jungwirth, P.; Devlin, J. P. Water Surface Is Acidic. *Proc. Natl. Acad. Sci. U. S. A.* **2007**, *104*, 7342–7347.
- [10] Beattie, J. K.; Djerdjev, A. M.; Warr, G. G. The Surface of Neat Water Is Basic. *Faraday Discuss.* **2009**, *141*, 31–39.
- [11] Mishra, H.; Enami, S.; Nielsen, R. J.; Stewart, L. A.; Hoffmann, M. R.; Goddard III, W. A.; Colussi, A. J. Brønsted Basicity of the Air–Water Interface. *Proc. Natl. Acad. Sci. U. S. A.* **2012**, *109*, 18679–18683.
- [12] Saykally, R. J. Two Sides of the Acid–Base Story. *Nat. Chem.* **2013**, *5*, 82–84.
- [13] Quincke, G. Ueber die Fortführung materieller Theilchen durch strömende Elektrizität. *Ann. Phys.* **1861**, *189*, 513–598.
- [14] Graciaa, A.; Morel, G.; Saulner, P.; Lachaise, J.; Schechter, R. The ζ -Potential of Gas Bubbles. *J. Colloid Interface Sci.* **1995**, *172*, 131–136.
- [15] Creux, P.; Lachaise, J.; Graciaa, A.; Beattie, J. K.; Djerdjev, A. M. Strong Specific Hydroxide Ion Binding at the Pristine Oil/Water and Air/Water Interfaces. *J. Phys. Chem. B* **2009**, *113*, 14146–14150.
- [16] Creux, P.; Lachaise, J.; Graciaa, A.; Beattie, J. K. Specific Cation Effects at the Hydroxide-Charged Air/Water Interface. *J. Phys. Chem. C* **2007**, *111*, 3753–3755.
- [17] Marinova, K.; Alargova, R.; Denkov, N.; Velev, O.; Petsev, D.; Ivanov, I.; Borwankar, R. Charging of Oil-Water Interfaces Due to Spontaneous Adsorption of Hydroxyl Ions. *Langmuir* **1996**, *12*, 2045–2051.
- [18] Beattie, J. K.; Djerdjev, A. M. The Pristine Oil/Water Interface: Surfactant-Free Hydroxide-Charged Emulsions. *Angew. Chem. Int. Ed.* **2004**, *43*, 3568–3571.
- [19] Fang, H.; Wu, W.; Sang, Y.; Chen, S.; Zhu, X.; Zhang, L.; Niu, Y.; Gan, W. Evidence of the Adsorption of Hydroxide Ion at Hexadecane/Water Interface from Second Harmonic Generation Study. *RSC Adv.* **2015**, *5*, 23578–23585.
- [20] Tian, C. S.; Shen, Y. R. Structure and Charging of Hydrophobic Material/Water Interfaces Studied by Phase-Sensitive Sum-Frequency Vibrational Spectroscopy. *Proc. Natl. Acad. Sci. U. S. A.* **2009**, *106*, 15148–53.
- [21] Yang, S.; Chen, M.; Su, Y.; Xu, J.; Wu, X.; Tian, C. Stabilization of Hydroxide Ions at the Interface of a Hydrophobic Monolayer on Water via Reduced Proton Transfer. **2020**, *125*, 156803.
- [22] Petersen, P. B.; Saykally, R. J. Evidence for an Enhanced Hydronium Concentration at the Liquid Water Surface. *J. Phys. Chem. B* **2005**, *109*, 7976–7980.
- [23] Das, S.; Imoto, S.; Sun, S.; Nagata, Y.; Backus, E. H.; Bonn, M. Nature of Excess Hydrated Proton at the Water–Air Interface. *J. Am. Chem. Soc.* **2019**, *142*, 945–952.
- [24] Chiang, K.-Y.; Dalstein, L.; Wen, Y.-C. Affinity of Hydrated Protons at Intrinsic Water/Vapor Interface Revealed by Ion-Induced Water Alignment. *J. Phys. Chem. Lett.* **2020**, *11*, 696–701.
- [25] Petersen, M. K.; Iyengar, S. S.; Day, T. J.; Voth, G. A. The Hydrated Proton at the Water Liquid/Vapor Interface. *J. Phys. Chem. B* **2004**, *108*, 14804–14806.
- [26] Lee, H.-S.; Tuckerman, M. E. *Ab Initio* Molecular Dynamics Studies of the Liquid–Vapor Interface of an HCl Solution. *J. Phys. Chem. A* **2009**, *113*, 2144–2151.
- [27] Hub, J. S.; Wolf, M. G.; Coleman, C.; van Maaren, P. J.; Groenhof, G.; van der Spoel, D. Thermodynamics of Hydronium and Hydroxide Surface Solvation. *Chem. Sci.* **2014**, *5*, 1745–1749.
- [28] Tse, Y.-L. S.; Chen, C.; Lindberg, G. E.; Kumar, R.; Voth, G. A. Propensity of Hydrated Excess Protons and Hydroxide Anions for the Air–Water Interface. *J. Am. Chem. Soc.* **2015**, *137*, 12610–12616.
- [29] Mamakulov, S. I.; Allolio, C.; Netz, R. R.; Bonthuis, D. J. Orientation-Induced Adsorption of Hydrated Protons at the Air–Water Interface. *Angew. Chem. Int. Ed.* **2017**, *56*, 15846–15851.
- [30] Li, Z.; Li, C.; Wang, Z.; Voth, G. A. What Coordinate Best Describes the Affinity of the Hydrated Excess Proton for the Air–Water Interface? *J. Phys. Chem. B* **2020**, *124*, 5039–5046.
- [31] de la Puente, M.; Laage, D. How the Acidity of Water Droplets and Films Is Controlled by the Air–Water Interface. *J. Am. Chem. Soc.* **2023**, *145*, 25186–25194.
- [32] Baer, M. D.; Kuo, I.-F. W.; Tobias, D. J.; Mundy, C. J. Toward a Unified Picture of the Water Self-Ions at the Air–Water Interface: A Density Functional Theory Perspective. *J. Phys. Chem. B* **2014**, *118*, 8364–8372.
- [33] Mundy, C. J.; Kuo, I.-F. W.; Tuckerman, M. E.; Lee, H.-S.; Tobias, D. J. Hydroxide Anion at the Air–Water Interface. *Chem. Phys. Lett.* **2009**, *481*, 2–8.
- [34] Bai, C.; Herzfeld, J. Surface Propensities of the Self-Ions of Water. *ACS Cent. Sci.* **2016**, *2*, 225–231.
- [35] Zhang, P.; Feng, M.; Xu, X. Double-Layer Distribution of Hydronium and Hydroxide Ions in the Air–Water Interface. *ACS Phys. Chem. Au* **2024**, *4*, 336–346.
- [36] Zhang, P.; Chen, C.; Feng, M.; Sun, C.; Xu, X. Hydroxide and Hydronium Ions Modulate the Dynamic Evolution of Nitrogen Nanobubbles in Water. *J. Am. Chem. Soc.* **2024**, *146*, 19537–19546.
- [37] Litman, Y.; Chiang, K.-Y.; Seki, T.; Nagata, Y.; Bonn, M. Surface Stratification Determines the Interfacial Water Structure of Simple Electrolyte Solutions. *Nat. Chem.* **2024**, 644–650.

- [38] Eigen, M.; De Maeyer, L. Untersuchungen über die Kinetik der Neutralisation. I. Z. Elektrochem., Ber. Bunsenges. Phys. Chem. **1955**, *59*, 986–993.
- [39] Eigen, M.; De Maeyer, L. Self-Dissociation and Protonic Charge Transport in Water and Ice. Proc. R. Soc. London, Ser. A **1958**, *247*, 505–533.
- [40] Åqvist, J.; Warshel, A. Simulation of Enzyme Reactions Using Valence Bond Force Fields and Other Hybrid Quantum/Classical Approaches. Chem. Rev. **1993**, *93*, 2523–2544.
- [41] Trout, B. L.; Parrinello, M. The Dissociation Mechanism of H₂O in Water Studied by First-Principles Molecular Dynamics. Chem. Phys. Lett. **1998**, *288*, 343–347.
- [42] Geissler, P. L.; Dellago, C.; Chandler, D.; Hutter, J.; Parrinello, M. Autoionization in Liquid Water. Science **2001**, *291*, 2121–2124.
- [43] Hassanali, A.; Prakash, M. K.; Eshet, H.; Parrinello, M. On the Recombination of Hydronium and Hydroxide Ions in Water. Proc. Natl. Acad. Sci. U. S. A. **2011**, *108*, 20410–20415.
- [44] Moqadam, M.; Lervik, A.; Riccardi, E.; Venkatraman, V.; Alsborg, B. K.; van Erp, T. S. Local Initiation Conditions for Water Autoionization. Proc. Natl. Acad. Sci. U. S. A. **2018**, *115*, E4569–E4576.
- [45] Di Pino, S.; Perez Sirkin, Y. A.; Morzan, U. N.; Sánchez, V. M.; Hassanali, A.; Scherlis, D. A. Water Self-Dissociation Is Insensitive to Nanoscale Environments. Angew. Chem. **2023**, *135*, e202306526.
- [46] Liu, L.; Tian, Y.; Yang, X.; Liu, C. Mechanistic Insights into Water Autoionization Through Metadynamics Simulation Enhanced by Machine Learning. Phys. Rev. Lett. **2023**, *131*, 158001.
- [47] Calegari Andrade, M.; Car, R.; Selloni, A. Probing the Self-Ionization of Liquid Water With *Ab Initio* Deep Potential Molecular Dynamics. Proc. Natl. Acad. Sci. U. S. A. **2023**, *120*, e2302468120.
- [48] Dasgupta, S.; Cassone, G.; Paesani, F. Nuclear Quantum Effects and the Grotthuss Mechanism Dictate the pH of Liquid Water. ChemRxiv **2024**.
- [49] Invernizzi, M.; Parrinello, M. Rethinking Metadynamics: From Bias Potentials to Probability Distributions. J. Phys. Chem. Lett. **2020**, *11*, 2731–2736.
- [50] Invernizzi, M.; Parrinello, M. Exploration vs Convergence Speed in Adaptive-Bias Enhanced Sampling. J. Chem. Theory Comput. **2022**, *18*, 3988–3996.
- [51] Grifoni, E.; Piccini, G.; Parrinello, M. Microscopic Description of Acid-Base Equilibrium. Proc. Natl. Acad. Sci. U. S. A. **2019**, *116*, 4054–4057.
- [52] Grifoni, E.; Piccini, G.; Parrinello, M. Tautomeric Equilibrium in Condensed Phases. J. Chem. Theory Comput. **2020**, *16*, 6027–6031.
- [53] Zhang, P.; Gardini, A. T.; Xu, X.; Parrinello, M. Intramolecular and Water Mediated Tautomerism of Solvated Glycine. J. Chem. Inf. Model. **2024**, *64*, 3599–3604.
- [54] Zhao, Y.; Truhlar, D. G. The M06 Suite of Density Functionals for Main Group Thermochemistry, Thermochemical Kinetics, Noncovalent Interactions, Excited States, and Transition Elements: Two New Functionals and Systematic Testing of Four M06-Class Functionals and 12 Other Functionals. Theor. Chem. Acc. **2008**, *120*, 215–241.
- [55] Villard, J.; Bircher, M. P.; Rothlisberger, U. Structure and Dynamics of Liquid Water from *Ab Initio* Simulations: Adding Minnesota Density Functionals to Jacob’s Ladder. Chem. Sci. **2024**, 4434–4451.
- [56] Giroday, T.; Montero-Campillo, M. M.; Mora-Diez, N. Thermodynamic Stability of PFOS: M06-2X and B3LYP Comparison. Comput. Theor. Chem. **2014**, *1046*, 81–92.
- [57] Chen, Y.; Zhang, L.; Wang, H.; E, W. DeePKS: A Comprehensive Data-Driven Approach Toward Chemically Accurate Density Functional Theory. J. Chem. Theory Comput. **2020**, *17*, 170–181.
- [58] Chen, Y.; Zhang, L.; Wang, H.; Weinan, E. DeePKS-kit: A Package for Developing Machine Learning-Based Chemically Accurate Energy and Density Functional Models. Comput. Phys. Commun. **2023**, *282*, 108520.
- [59] Li, W.; Ou, Q.; Chen, Y.; Cao, Y.; Liu, R.; Zhang, C.; Zheng, D.; Cai, C.; Wu, X.; Wang, H.; Chen, M.; Zhang, L. DeePKS+ABACUS as a Bridge Between Expensive Quantum Mechanical Models and Machine Learning Potentials. J. Phys. Chem. A **2022**, *126*, 9154–9164.
- [60] Wang, H.; Zhang, L.; Han, J.; E, W. DeePMD-kit: A Deep Learning Package for Many-Body Potential Energy Representation and Molecular Dynamics. Comput. Phys. Commun. **2018**, *228*, 178–184.
- [61] Zeng, J. et al. DeePMD-kit v2: A Software Package for Deep Potential Models. J. Chem. Phys. **2023**, *159*, 054801.
- [62] de Grotthuss, C. J. T. Mémoire sur la Décomposition de l’Eau et des Corps qu’elle Tient en Dissolution à l’Aide de l’Électricité Galvanique. Ann. Chim. **1806**, 54–74.
- [63] Marx, D. Proton Transfer 200 Years after von Grotthuss: Insights from *Ab Initio* Simulations. ChemPhysChem **2006**, *7*, 1848–1870.
- [64] Natzle, W. C.; Moore, C. B. Recombination of H⁺ and OH[−] in Pure Liquid Water. J. Phys. Chem. **1985**, *89*, 2605–2612.
- [65] Luz, Z.; Meiboom, S. The Activation Energies of Proton Transfer Reactions in Water. J. Am. Chem. Soc. **1964**, *86*, 4768–4769.
- [66] Agmon, N.; Bakker, H. J.; Campen, R. K.; Henchman, R. H.; Pohl, P.; Roke, S.; Thaömer, M.; Hassanali, A. Protons and Hydroxide Ions in Aqueous Systems. Chem. Rev. **2016**, *116*, 7642–7672.
- [67] Du, Q.; Freysz, E.; Shen, Y. R. Vibrational Spectra of Water Molecules at Quartz/Water Interfaces. Phys. Rev. Lett. **1994**, *72*, 238.
- [68] Inoue, K.-i.; Nihonyanagi, S.; Singh, P. C.; Yamaguchi, S.; Tahara, T. 2D Heterodyne-Detected Sum Frequency Generation Study on the Ultrafast Vibrational Dynamics of H₂O and HOD Water at Charged Interfaces. J. Chem. Phys. **2015**, *142*, 212431.
- [69] Ishiyama, T.; Morita, A. Computational Analysis of Vibrational Sum Frequency Generation Spectroscopy. Annu. Rev. Phys. Chem. **2017**, *68*, 355–377.
- [70] Tang, F.; Ohto, T.; Sun, S.; Rouxel, J. R.; Imoto, S.; Backus, E. H.; Mukamel, S.; Bonn, M.; Nagata, Y. Molecular Structure and Modeling of Water-Air and Ice-Air Interfaces Monitored by Sum-Frequency Generation. Chem. Rev. **2020**, *120*, 3633–3667.
- [71] Sakunkaewkasem, S.; Deleon, D.; Choi, Y.; Tran, H.-V.; Marquez, M. D.; Baldelli, S.; Lee, T. R. Sum Frequency Generation Spectroscopy of Fluorinated Organic Material-Based Interfaces: A Tutorial Review. Analyst **2023**, *148*, 2901–2920.
- [72] Hirshfeld, F. L. Bonded-Atom Fragments for Describing Molecular Charge Densities. Theor., Chim. Acta **1977**, *44*, 129–138.
- [73] Zeng, Q.; Chen, B.; Yu, X.; Zhang, S.; Kang, D.; Wang, H.; Dai, J. Towards Large-Scale and Spatiotemporally Resolved Diagnosis of Electronic Density of States by Deep Learning. Phys. Rev. B **2022**, *105*, 174109.
- [74] Zhang, D.; Bi, H.; Dai, F.-Z.; Jiang, W.; Liu, X.; Zhang, L.; Wang, H. Pretraining of Attention-Based Deep Learning Potential Model for Molecular Simulation. Npj Comput. Mater **2024**, *10*, 94.
- [75] Zhang, L.; Han, J.; Wang, H.; Car, R.; Weinan, E. Deep Potential Molecular Dynamics: A Scalable Model With the Accuracy of Quantum Mechanics. Phys. Rev. Lett. **2018**, *120*, 143001.
- [76] Kühne, T. D. et al. CP2K: An Electronic Structure and Molecular Dynamics Software Package-Quickstep: Efficient and Accurate Electronic Structure Calculations. J. Chem. Phys. **2020**, *152*, 194103.
- [77] Goedecker, S.; Teter, M.; Hutter, J. Separable Dual-Space Gaussian Pseudopotentials. Phys. Rev. B **1996**, *54*, 1703.
- [78] Hartwigsen, C.; Goedecker, S.; Hutter, J. Relativistic Separable Dual-Space Gaussian Pseudopotentials from H to Rn. Phys. Rev. B **1998**, *58*, 3641.
- [79] VandeVondele, J.; Krack, M.; Mohamed, F.; Parrinello, M.; Chassaing, T.; Hutter, J. Quickstep: Fast and Accurate Density Functional Calculations Using a Mixed Gaussian and Plane Waves Approach. Comput. Phys. Commun. **2005**, *167*, 103–128.
- [80] Guidon, M.; Hutter, J.; VandeVondele, J. Auxiliary Density Matrix Methods for Hartree-Fock Exchange Calculations. J. Chem. Theory Comput. **2010**, *6*, 2348–2364.
- [81] Plimpton, S. Fast Parallel Algorithms for Short-Range Molecular Dynamics. J. Comput. Phys. **1995**, *117*, 1–19.
- [82] Bussi, G.; Donadio, D.; Parrinello, M. Canonical Sampling Through Velocity Rescaling. J. Chem. Phys. **2007**, *126*, 014101.
- [83] Invernizzi, M.; Piaggi, P. M.; Parrinello, M. Unified Approach to Enhanced Sampling. Phys. Rev. X **2020**, *10*, 041034.
- [84] Tribello, G. A.; Bonomi, M.; Branduardi, D.; Camilloni, C.; Bussi, G. PLUMED 2: New Feathers for an Old Bird. Comput. Phys. Commun. **2014**, *185*, 604–613.

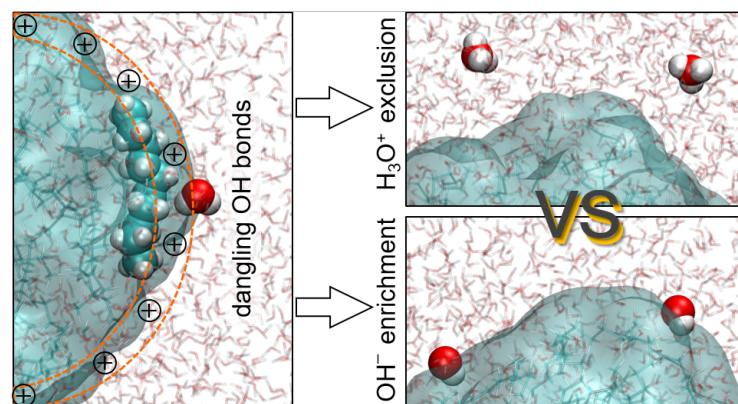


Table of contents (TOC)